Secondary instabilities in the shear layer of a compressible jet over a convex wall

Qing Wang, Feng Qu,* Zeyu Wang, Di Sun, and Junqiang Bai
School of Aeronautics, Northwestern Polytechnical University, Xi'an 710072, China

(Received 1 March 2023; accepted 6 September 2023; published 5 October 2023)

The compressible jet over a convex wall is numerically studied using the delayed detached-eddy simulation method based on the two-equation shear-stress transport model. In particular, the current study focuses on the secondary instabilities in the shear layer. The results show that the alternating high-speed and low-speed streaks in the shear layer induced by the streamwise vortices exhibit secondary instabilities similar to those found in other wall-bounded flows. The varicose mode secondary instability induces the thinning and thickening motions of the low-speed regions, whereas the sinuous mode leads to the side-to-side sway motions. The hairpin vortices and the counter-rotating roll-mode, which are often associated with the symmetric (varicose-type) mode, are dominated in the transient stage of the shear layer. However, as the shear layer evolves downstream, there still appear one-sided roll-modes and quasistreamwise vortices with vorticity of alternate sign produced by the spanwise overlapping of the hairpin vortex legs, which are well known to be related to the antisymmetric (sinuous-type) mode. Further, the dynamic mode decomposition analysis performed on the spanwise velocity fluctuation of the instantaneous snapshots reveals the presence of both sinuous- and varicose-type secondary instabilities, as well as their competitions, in the shear layer. Quantitatively, from $\theta = 25^\circ$ to $\theta = 45^\circ$, the proportion of the varicose mode decreases from 84.4% to 50.6%, and accordingly, the sinuous mode increases from 15.6% to 49.4%. The analysis of the turbulent kinetic energy production terms reveals that both varicose and sinuous modes are influenced by the radial and spanwise shear components of the turbulent energy production term, and they are in the same order of magnitude. Additionally, the mechanism of the instability is due to the velocity fluctuations and Reynolds stress parallel to the local mean flow gradient. The local inflection point instability caused by the mean flow gradient is also the source of turbulent energy that sustains the instabilities.

DOI: 10.1103/PhysRevFluids.8.103901

I. INTRODUCTION

When a jet ejects tangentially over a convex wall, it remains attached due to the Coanda effect [1] rather than instantly detaches from the convex wall. Coanda wall jet finds successful application in aircraft design as circulation control devices to achieve the lift augmentation or roll control [2–12]. In such an application, the Coanda jet is used to inject momentum and entrain the external flow to deflect with the jet, so the goal is to enable the mixing of high momentum Coanda jet. However, the deployment of this technology to a full-size aircraft still faces several obstacles, particularly given the low control effectiveness of supersonic jet with transonic freestream [13]. Thus, it requires a thorough understanding of the fluid mechanics of the supersonic jet over a convex wall and the turbulence field it generates.

*qufeng@nwpu.edu.cn

In the instabilities of the jet over a convex wall, the inner layer close to the wall exhibits Tollmien-Schlichting viscous instability such as a Blasius boundary layer [14,15]. The outer part exits an inflection point of. the velocity profile, which would grow and roll up spanwise vortices through Kelvin-Helmholtz instability [16,17]. Apart from these instabilities above, another instability, centrifugal instability is also introduced in the outer part of the jet due to the addition of the surface curvature [18–20]. This leads to the generation of the streamwise vortices according to the observation of several centrifugally unstable flows, such as Taylor-Couette flow [21], curved channel flow (Dean flow), [22] and concave boundary layer (Görtler flow) [23]. The streamwise vortices in these flows create the spanwise and radial inflection points of the velocity profiles, which support to trigger the secondary instabilities of the longitudinal streaks. There are two common types of secondary instabilities, varicose and sinuous instability mode, which are identified by symmetric and antisymmetric patterns appearing in the spanwise direction with respect to the low-speed streak in the shear flow [24–27]. The development of the varicose instability results in the generation of the hairpin vortex, while the sinuous instability leads to quasistreamwise vortices with vorticity of alternate signs [28–30]. Studies have shown that inflection points in the spanwise and wall-normal profiles are usually related to sinuous and varicose instabilities, respectively. Another secondary instability, known as Eckhaus instability [31], causes the unsteadiness of the streamwise vortices with merging and splitting tendency of the vortices [32]. In general, secondary instabilities in these wall-bounded shear flows have been thoroughly researched, and they are now recognized as a key component in the transition to turbulence.

The secondary instabilities mentioned above are also expected to be active in the jet over a convex wall. For the incompressible convex wall jet, researchers have found that the growth rate and turbulent fluctuations in the curved wall jet were much greater than those in the plane wall jet [33]. This enhancement was then confirmed to be caused by the centrifugal instability induced streamwise vortices [16,34–36]. Later, these streamwise vortices were observed using flow visualization and Particle Image Velocimetry, and they were found to be highly unsteady due to the wavy secondary instability [37]. Recently, Pandey *et al.* [38] have confirmed the existence of the wavy secondary instability in a forced jet over a convex wall by proper orthogonal decomposition [39] analysis of the spanwise velocity fluctuation. Also, Pandey and Gregory [40] found the merging and splitting of the streamwise vortices to match the scale of the spanwise wavelength and the local jet half-width in the forced convex wall jet [34]. This spanwise wavelength selection is presumably a form of Eckhaus instability. This instability, in conjunction with the wavy instability, is believed to play an important role in the development of the incompressible convex wall jet. However, in compressible situations, their characteristics are not well known. Our previous numerical study on the supersonic jet over a convex wall observed the spanwise periodic high-speed and low-speed streaks in the shear layer, which are attributed to the streamwise vortices induced by centrifugal instability. Their dynamic mode decomposition (DMD) [41] analysis of the streamwise vorticity fields in the cross-stream plane revealed a side-to-side sway motion of the streamwise vortices, which indicated the existence of the secondary instability in the shear layer [42]. However, there is still a scarcity of in-depth and quantitative research on the secondary instability in the shear layer of a convex wall jet. This is particularly significant to understand the instability procedure of the shear layer in the compressible convex wall jet.

This paper is a continuation of our previous work [42], aiming to understand the mechanism of secondary instability in the shear layer. The most common method for studying secondary instabilities is to employ symmetric or antisymmetric disturbances to induce a pure varicose or sinuous instability [25,26,29]. Actually, there may be a combination and competition of all types of instability modes in the actual flow [29,38], which makes the situation much more complicated. Thus, the delayed detached-eddy simulation (DDES) method, which is the hybrid of the Reynolds-averaged Navier-Stokes (RANS) and large-eddy simulation (LES), is employed to make a nonlinear simulation of the convex wall jet. It could avoid the massive computational cost of direct numerical simulation or LES with near wall resolution methods in the boundary layer [43]. By adding certain conditions to the sorting or averaging process [44,45], we can quantitatively examine the secondary

instability modes and gain a further insight into the instability mechanisms in the shear layer. The organization of this paper is as follows: Section II describes the details of numerical methods. In Sec. III, computational details are described. Numerical results and analysis are presented in Sec. IV. The last section contains the main conclusions.

II. NUMERICAL METHODS

All numerical simulations in this study are conducted by an in-house three-dimensional cell-centered finite volume solver developed by the authors. The solver has been successfully applied to considerable numerical studies on subsonic flows [46], supersonic flows [47,48], hypersonic flows [49,50], and supersonic Coanda flow [42,51]. For simplicity, the main algorithms of the solver are represented as follows.

A. Delayed detached-eddy simulation

The basic governing equations are the RANS equations. For the additional Reynolds stress in the RANS equations, researchers have constructed many turbulence models to solve it. The shear-stress transport (SST) [52] turbulence model is adopted in this paper.

The two-equation SST DDES method is implemented by modifying the dissipation-rate term of the turbulent kinetic energy transport equation as follows:

$$\frac{\partial(\rho k)}{\partial t}+\frac{\partial(\rho U_i k)}{\partial x_i}=\tilde{P}_k-\frac{\rho k^{3/2}}{l_{\text{hybrid}}}+\frac{\partial}{\partial x_i}\left[(\mu+\sigma_k\mu_t)\frac{\partial k}{\partial x_i}\right] \tag{1}$$

$$\frac{\partial(\rho\omega)}{\partial t}+\frac{\partial(\rho U_i\omega)}{\partial x_i}=\frac{\gamma}{\nu_t}\tilde{P}_k-\beta\rho\omega^2+\frac{\partial}{\partial x_i}\left[(\mu+\sigma_\omega\mu_t)\frac{\partial\omega}{\partial x_i}\right]+2(1-F_1)\rho\frac{\sigma_{\omega 2}}{\omega}\frac{\partial k}{\partial x_i}\frac{\partial\omega}{\partial x_i}, \tag{2}$$

where k and ω represent the turbulent kinetic energy and specific dissipation rate, respectively. ρ is the density, μ the viscosity, γ the specific heat ratio, σ_k and σ_ω are diffusion coefficients of k and ω, and $\tilde{P}_k$ the production term of turbulent kinetic energy. β is a constant, and the value of β is recommended as 0.09 by Menter [52]. l_{hybrid} is the length scale defined as:

$$l_{\text{hybrid}}=\min\{l_{\text{RANS}},l_{\text{LES}}\}, \tag{3}$$

$$l_{\text{RANS}}=\frac{k^{1/2}}{\beta\omega},\ l_{\text{LES}}=C_{\text{DES}}\Delta=C_{\text{DES}}\max\{\Delta_x,\Delta_y,\Delta_z\}, \tag{4}$$

in which l_{RANS} and l_{LES} are the length scales of the RANS turbulence model and LES method, respectively. Δ is the grid scale, which is equal to the maximum grid spacing in x, y, and z directions for the structured grid. C_{DES} is an empirical constant that needs to be calibrated and verified, reflecting the degree of dissipation in different CFD codes. As for the SST turbulence model, $C_{\text{DES}}=(1-F_1)C_{\text{DES}}^{\text{outer}}+F_1C_{\text{DES}}^{\text{inner}}$, where $C_{\text{DES}}^{\text{outer}}$ is equal to 0.61, the $C_{\text{DES}}^{\text{inner}}$ is equal to 0.78, and the F_1 is the internal function [43] in the SST turbulence model.

However, the DES method exists the modeled-stress depletion which will produce the grid induced separation. To overcome this problem, Spalart *et al.* [43] proposed a new method named DDES by constructing a delayed function. The length scale of DDES can be expressed as follows:

$$\left.\begin{aligned} l_{\text{hybrid}}&=l_{\text{RANS}}-f_d\max\{0,l_{\text{RANS}}-l_{\text{LES}}\}\\ f_d&=1-\tanh[(8r_d)^3]\\ r_d&=\frac{\nu+\nu_t}{\sqrt{u_{i,j}u_{i,j}}\kappa^2d^2}\end{aligned}\right\}, \tag{5}$$

where the f_d is the delayed function, ν_t is the kinematic eddy viscosity, ν is the molecular viscosity, $u_{i,j}$ are the velocity gradients, κ is the Kármán constant of 0.41, and d is the distance to the wall. The structure of the delay function and the meaning of the parameters are detailed in Ref. [43]. In case

the f_d tends to 0, the RANS calculation is used. And in case the f_d tends to 1, the DDES method is converted to the traditional DES method.

B. Numerical issues

Spatial discretization resolution is critical for a high-fidelity numerical simulation. To level down the numerical dissipation, the inviscid fluxes are computed via a Roe flux-difference upwind scheme with a fifth-order weighted essential nonoscillatory [53]. The viscous fluxes are discretized by a fourth-order central differencing scheme. The fully implicit lower upper-symmetric Gauss-Seidel time-marching scheme [54] with a second-order dual time-stepping method and Newton's subiteration for the inner loop is employed for time marching to achieve unsteady simulation.

In order to accelerate the formation of unsteady turbulent motions, all unsteady DDES simulations were initialized with corresponding converged steady RANS solutions. The unsteady DDES calculations are implemented with a fixed physical time-step size of 1.44×10^{-7} s. A maximum of 10 subiterations per time step were used, resulting in a residual drop of at least two to three orders. After the transient flow with 25 000 steps, the remaining 8000 steps are taken to obtain sufficient unsteady flow data per 25 steps for statistical analysis. The total physical time of 8000 steps allows the fluid to flow over 2.5 times the arc length of the convex wall at the characteristic velocity (sound speed) to ensure that the periodic motions of the typical coherent structures can be effectively captured.

III. COMPUTATIONAL DETAILS

This paper is a continuation of our previous work. The computational details were described in Wang *et al.* [42]. For brevity, we recall the main details here.

A. Model, flow conditions, and boundary conditions

The apparatus used in this study includes a convergent-divergent nozzle and a curved Coanda surface. The convergent-divergent nozzle is designed using a quasi-one-dimensional method based on isentropic flow theory without boundary layer corrections. The geometric tangency of the positions (i.e., the throat, the connection between the nozzle exit and Coanda surface), where the area changes, are ensured to eliminate the influence of geometric mutation on the flow. In addition, a symmetrical shape is used in upper and lower nozzle surfaces. The nozzle exit height is 10 mm, and the design point of the nozzle pressure ratio is 7 ($\mathrm{NPR}_d = 7$). The Coanda surface is a 90° circular arc with a radius of 100 mm fixing the h/R ratio to 0.1. Experiments were conducted by Llopis-Pascual [55] at the University of Manchester. They obtained the pressure coefficient distribution of the Coanda surface and the Schlieren photograph of the jet. Unfortunately, no turbulence statistics of the jet were measured. As the experiments were carried out in quiescent air, the test conditions were $p_{\mathrm{amb}} = 100$ kPa, $T_{\mathrm{amb}} = 300$ K.

The geometric characteristics of the device and the cylindrical coordinate axes employed in this study are shown in Fig. 1. Azimuthal (θ), radial (y), and spanwise (z) coordinates correspond to the U, V, and W components of velocity, respectively. The jet half-width (y_2), which is the wall-normal location where the streamwise velocity is half ($0.5U_{\mathrm{max}}$) of its maximum value, is used as a measure of the jet thickness.

The detailed computational domain and boundary conditions were given in Wang *et al.* [42]. In particular,the inlet of the jet plenum is set to be the pressure inlet, where the NPR (the ratio of the nozzle total to static pressure) is specified ($p/p_{\mathrm{amb}} = \mathrm{NPR}$, $T/T_{\mathrm{amb}} = 1.2$).

B. Code validation and grid sensitivity

1. Code validation

A rectangular convergent-divergent nozzle flow [56] is presented for the solver validation. The nozzle had inlet, throat, and nozzle exit heights of 25.0, 13.1, and 15.75 mm. The axial lengths of

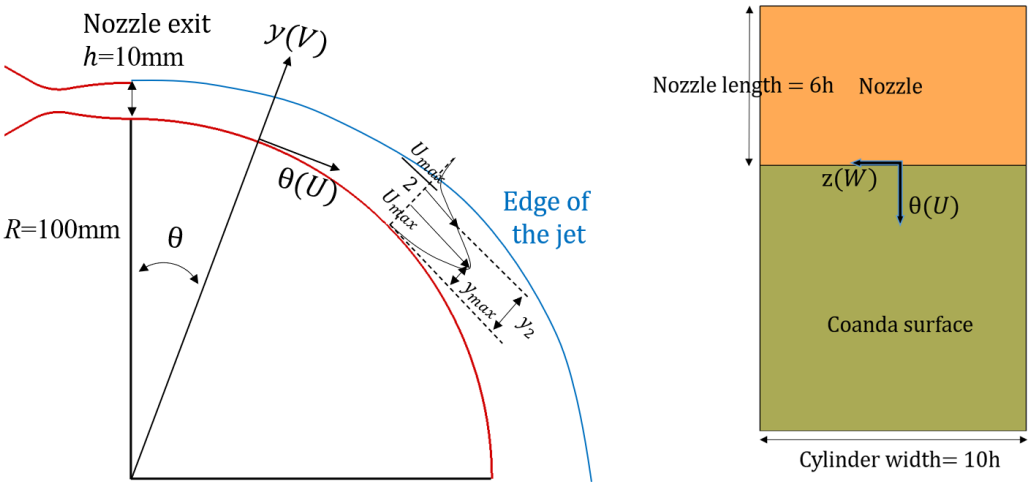

(a) side view (b) top view

FIG. 1. Schematics of the coordinate system

the convergent-divergent are 56.6 and 55.78 mm, respectively. The nozzle width remains constant at 91.6 mm. The nozzle exit lip thickness is chosen to be 1 mm. The throat hydraulic diameter ($D_h = 22.92$ mm) is chosen as the reference length. The designed nozzle pressure ratio is 4 ($\mathrm{NPR}_d = 4.0$, using inviscid approximation without considering the losses and inlet boundary-layer effects). Experiments were carried out in the High-Pressure Nozzle Test Facility at Loughborough University [56].

The computational grid is similar to that of the LES simulation of Wang *et al.* [57] on the same configuration. There are $201 \times 56 \times 101$ points on the major and minor axes at the nozzle exit in this study. The grid near the wall and the shear layer were refined to accurately solve flow structures there. A total of 20 million cells were used. The operating condition is an overexpanded NPR = 2.5. The converged steady RANS solution is used as the initial of unsteady DDES simulation. A fixed time step of 7.2×10^{-7} s is used for the calculation, and ten subiterations are required to reduce the residual at each physical time step at least two orders of magnitude. The first 10 000 time steps are employed to establish a statistically stationary state, and then statistics are gathered for the additional 10 000 time steps (about 6 solution domain flow through times). Figure 2 shows the schematics of the coordinate system and measured stations of Behrouzi *et al.*'s experiments [56].

Figure 3 shows that the predicted centreline axial velocity profile consistent with the measured data, which indicates that the solver in this paper can accurately solve the potential core length and the dissipation downstream. Figure 4 shows the comparison between the predicted and measured axial velocity profile at three streamwise stations shown in Fig. 2. Further, the comparison of axes velocity fluctuation rms is presented in Fig. 5. All mean velocity and turbulence data are normalized by a reference velocity taken as the centreline axial velocity at nozzle inlet (U_{ref}). In the region near the nozzle exit ($x/D_h = 1.0, 2.0$), both numerical velocity profiles and rms of the axes velocity fluctuation agree well with the measured results. As the jet develops further downstream ($x/D_h = 8.0$), the difference between numerical and experimental results increases, especially in the core region of the jet. This may be due to an increase in grid scale near the center of the jet. The large-scale grid may not accurately capture small-scale fluctuations in this region. However, the solver utilized in this study accurately predicted the peak values of velocity and turbulence fluctuations, and the development of the jet shear layer.

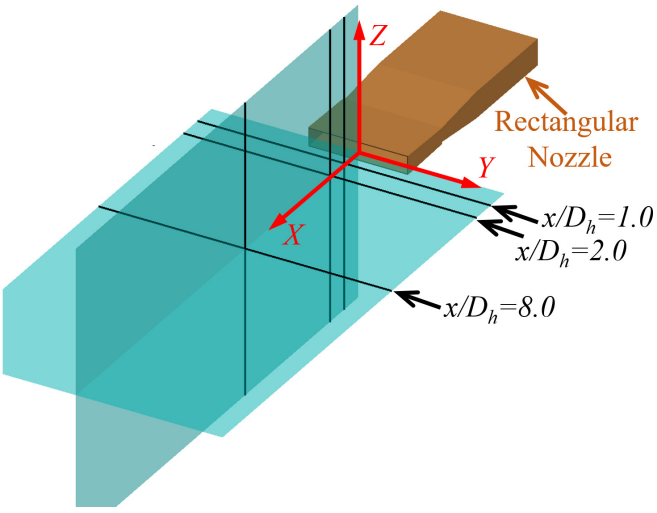

FIG. 2. Schematics of the coordinate system and measured stations of Behrouzi *et al.*'s experiments [56].

2. Grid sensitivity

The grid independence of the same apparatus and flow condition has finished in our published work [42]. For the integrity of this paper, the main results are summarized as follows: (1) Two mesh sizes were used to characterize the grid sensitivity of the solution. The coarse mesh contains $N_\theta \times N_y \times N_z = 251 \times 151 \times 121$ grids around the convex surface (resulting in a total of 6.6 million grids), while the fine mesh has $N_\theta \times N_y \times N_z = 301 \times 171 \times 151$ grids around the convex surface (resulting in total 10.5 million grids). By comparing the Mach contours, streamwise velocity profiles at various streamwise locations, development of the jet half-width, and vorticity thickness of the shear layer, the two meshes showed excellent grid independence. (2) In addition, the grid independence of the fine mesh was demonstrated by the following three aspects. First, for reliable DDES simulations, the grid size has to be adequately small to resolve the desired turbulent structures. The smallest Kolmogorov scale $\eta = (\nu^3/\varepsilon)^{1/4}$ is estimated to be about 0.04 mm in the jet mixing

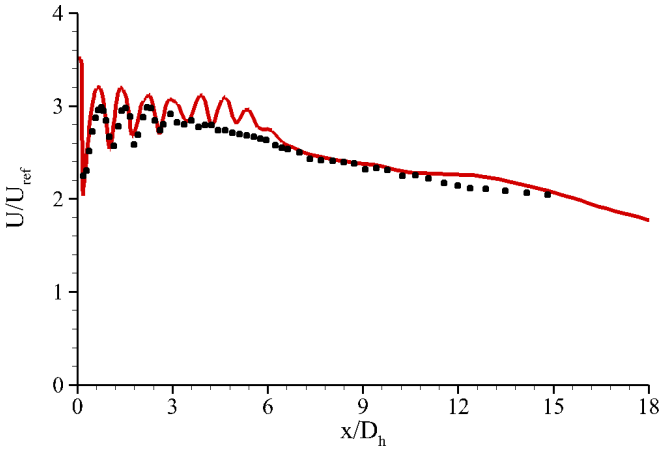

FIG. 3. Comparison between predicted and measured centreline axial velocity profile. Measured data of Behrouzi *et al.* [56]: symbols; DDES: line.

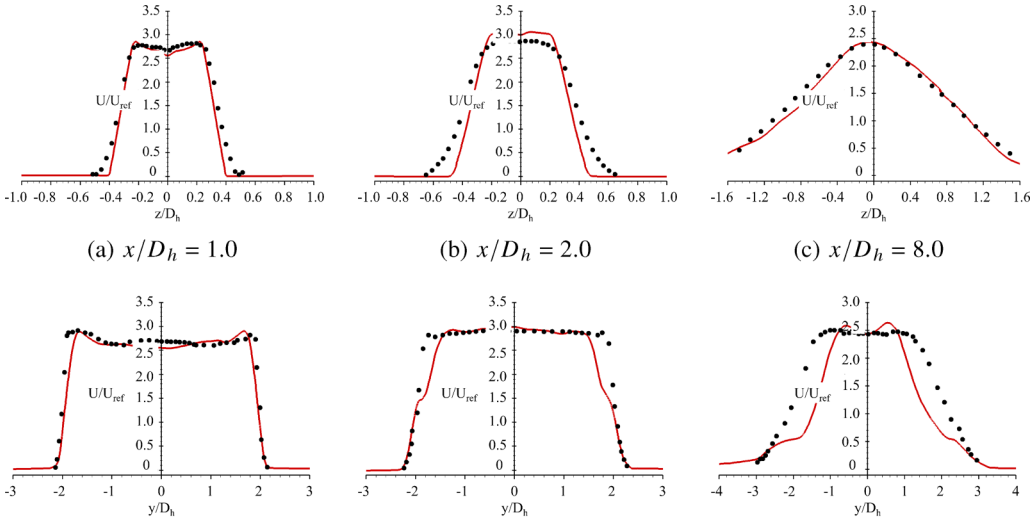

(a) $x/D_h = 1.0$ (b) $x/D_h = 2.0$ (c) $x/D_h = 8.0$

(d) $x/D_h = 1.0$ (e) $x/D_h = 2.0$ (f) $x/D_h = 8.0$

FIG. 4. Comparison between predicted and measured minor (top) and major (bottom) axes velocity profile. Measured data of Behrouzi *et al.* [56]: symbols; DDES: line.

layer center for the present simulations, and here ν and ε are the kinematic viscosity (calculated by Sutherland's law) and turbulent kinetic energy dissipation rate (estimated by RNG$k-\varepsilon$ model), respectively. The grid spacings around the jet mixing layer in (θ, y, z) directions are specified as (0.52, 0.05, 0.67) mm, which are about (12.5, 1.25, 17) times the Kolmogorov scale and are fine enough to resolve the jet mixing layer. Second, the computation domain in the z direction should be sufficiently wide to capture enough spanwise flow structures. The spanwise flow periodicity is well captured. Finally, the numerical pressure coefficient distribution on the Coanda well agrees with the experiment of Llopis-Pascual [55], which further proves the accuracy of the grid and solver in the present study. Thus, the resolution of fine mesh is considered to be sufficient for the unsteady numerical simulation and will be utilized in all the present investigations.

IV. RESULTS AND DISCUSSION

There are two important flow developing regions in the compressible jet over a convex wall, including the inner boundary layer region near the curved surface and the outer shear layer region. However, the overall purpose of this paper is to understand the secondary instabilities in the

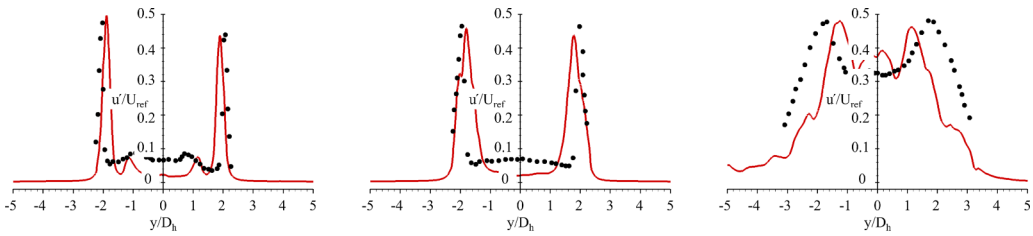

(a) $x/D_h = 1.0$ (b) $x/D_h = 2.0$ (c) $x/D_h = 8.0$

FIG. 5. Comparison between predicted and measured major rms of axes velocity fluctuation. Measured data of Behrouzi *et al.* [56]: symbols; DDES: line.

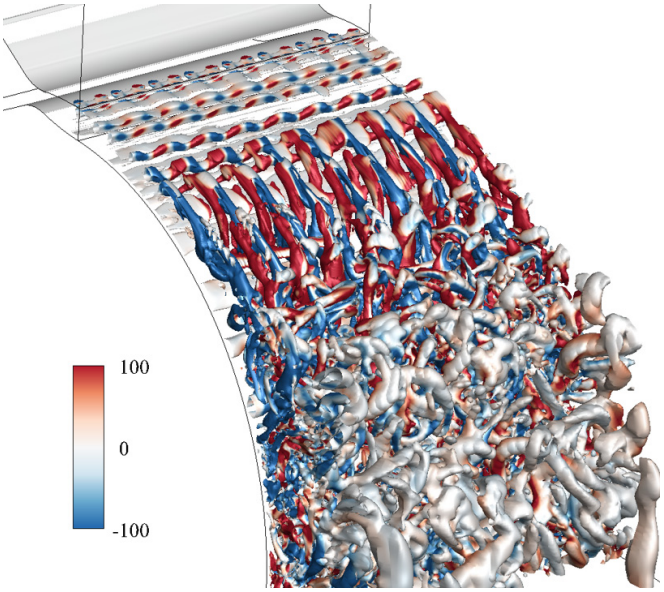

FIG. 6. Instantaneous vortex structures using Q criteria ($Q = 100$, colored by the streamwise vorticity).

outer shear layer, where Kelvin-Helmholtz-type inflectional instability and Taylor-Görtler-type centrifugal instability are dominant. The nozzle pressure ratio is specified as 3.0, resulting in a nozzle exit Mach number of 1.33 and the corresponding convective Mach number of 0.66. This is a moderately compressible condition according to the compression definition in the plane shear layer [58–61]. It should be noted that the Mach number and corresponding convective Mach number are characterized using the maximum value at the nozzle exit due to the flow nonuniformity.

A. Base flow

Figure 6 shows the instantaneous vortex structures using Q criteria, in which the iso-surface is colored by the streamwise vorticity. In the transition stage of the shear layer, the large-scale spanwise vortex tubes induced by the Kelvin-Helmholtz-type inflectional instability and the counter-rotating streamwise vortex tubes caused by the Taylor-Görtler-type centrifugal instability can be obviously observed. While in the fully developed region, the smaller-scale structures are dominant. In fact, our previous work [42] on the same configuration and flow condition has revealed a rapid growth rate of the shear layer in the transient region. Also, there is not only the self-similarity of the velocity profiles normalized by the jet half-width and local maximum velocity as that has been found in the incompressible jet over a convex wall by Neuendorf *et al.* [16] and Pandey *et al.* [38] but also self-similarity of normalized turbulent stresses in the fully developed region.

The counter-rotating streamwise vortices entrain the momentum exchange between the high-speed flow in the inner layer and the low-speed flow in the outer part of the shear layer. Figure 7 shows the ensemble averaged contours of the streamwise vorticity, streamwise velocity, and radial velocity at cross-stream plane $\theta = 35^\circ$. Under the action of the streamwise vortices, there are spanwise periodic upwash and downwash regions. The streamwise extension of these regions produces high-speed and low-speed streaks in the shear layer. In addition, the streamwise vortices generate inflection points in the spanwise and radial directions, which would trigger the secondary instabilities of streaks as those in other wall-bounded flows [24–27]. In fact, Pandey *et al.* [38] have observed the secondary instabilities in an incompressible convex wall jet.

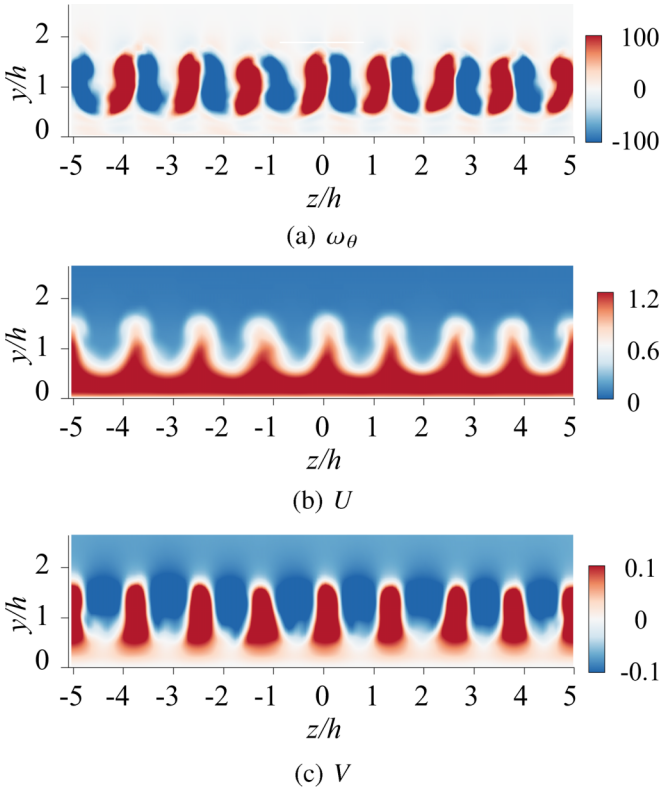

FIG. 7. Ensemble averaged contours of cross-stream plane at $\theta = 35°$, (a) streamwise vorticity, (b) streamwise velocity, and (c) radial velocity.

Figure 8 shows the radial and spanwise gradient of the streamwise velocity at $\theta = 35°$. The radial gradient has negative maximum in the downwash and upwash regions, which is associated with the largest negative spanwise vorticity. The spanwise gradient has an alternating positive and negative distribution, which is consistent with the streamwise vorticity shown in Fig. 7(a).

In order to further understand the scenario of the large coherent structures in the transient region of the shear layer, Fig. 9 shows instantaneous vortex structures of two neighbor low-speed streaks using Q criteria. It should be noted that the cylinder Coanda surface has been unfurled into abscissa, that is, the x axis represents the streamwise direction and the corresponding coordinate value is the azimuth angle of the cylindrical surface from the nozzle exit. Similarly, the ordinate in the figure corresponds to the radial distance from the cylinder surface and has been normalized by the nozzle exit height. It can be seen that the spanwise vortex tubes bend under the influence of the streamwise vortices. The streamwise vortex tubes, that is, two legs of the hairpin vortex, lie on

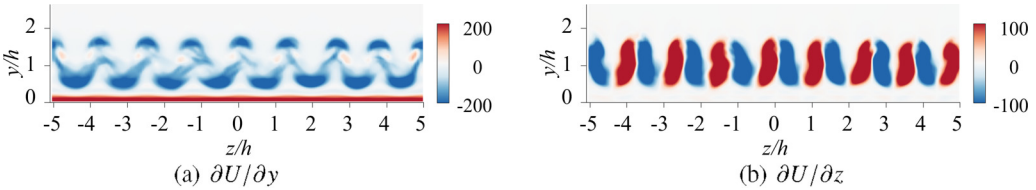

FIG. 8. Contours of (a) radial and (b) spanwise gradient of streamwise velocity at $\theta = 35°$.

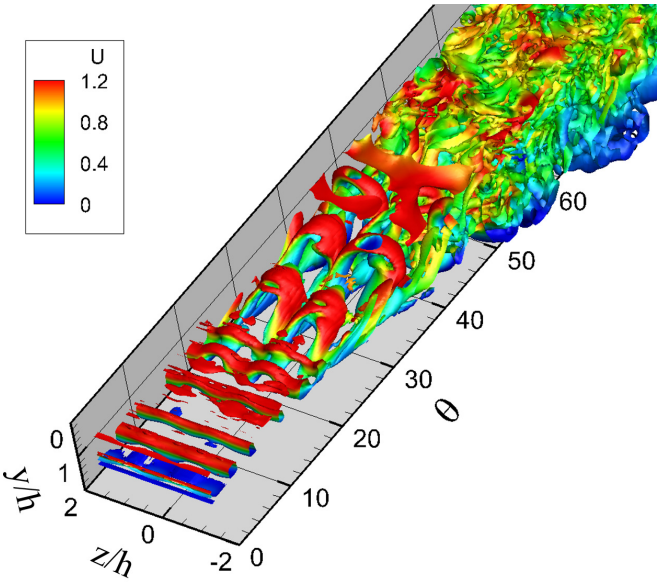

FIG. 9. Instantaneous vortex structures using Q criteria ($Q = 100$, colored by the streamwise velocity). A local view from the inner high-speed side.

the flanks of the low-speed streak and are connected by the spanwise vortex tube (the head of the hairpin vortex) on the high and low-speed streaks. The consistency between the streamwise vorticity [Fig. 7(a)] and the spanwise gradient of the streamwise velocity [Fig. 8(a)] distribution indicates that the streamwise vortices are generated at the location with the largest spanwise gradient. The two legs of the hairpin vortex are the results of the tilting action of the mean spanwise and radial shear on the spanwise vortex.

The above analysis of the shear layer represents the Görtler instability and the associated spanwise periodic streaks. Furthermore, the linear stability theory (LST) considered the compressible and curvature effects, which is developed by S. Scott Collis [62], is employed to the compressible jet over a convex wall in this paper. The method was described in detail in Ref. [62].

The code used in this study is validated using the spatially growing Tollmien-Schlichting waves in the boundary layer. The base flow is computed from the compressible Falkner-Skan-Cooke equations (see Appendix C in Ref. [62]). The flow conditions are $\mathrm{Ma} = 0.3$, $\mathrm{Re} = 1000$, and $\mathrm{Pr} = 1.0$ with the reference length scale of the displacement thickness. For two-dimensional disturbances of frequency $\omega = 0.08$, we predict the spatial wave number as $\alpha = 0.228050 - 0.0065090i$, which agrees well with the result of Collis [62], $\alpha = 0.228047 - 0.0065163i$. The comparison of the eigenfunction is shown in Fig. 10, which is consistent with Collis's result [62] as well.

The shear layer develops downstream in space, so the spatial problem was considered in this study. In the spatial problem, the frequency (ω) and the spanwise wave number (β) are specified real values and the remaining wave number (α) is the eigenvalue. The growth rate is given by the imaginary part of α, while the wave number is given by the real part of α. In order to obtain a linear stability map, the mean velocity profile of the DDES simulation near the nozzle exit shown in Fig. 11(a) was used to solve the stability equations. In this analysis, the reference velocity and length are the ambient air sound speed a_∞ and the nozzle exit height h, respectively. We are most interested in the unstable mode of the shear layer, in which the eigenfunction of the disturbances should be distributed in the shear layer. Figure 11(b) shows the eigenfunction profile of the streamwise velocity disturbance for the unstable mode in the shear layer ($\omega = 0.1$, $\beta = 0$).

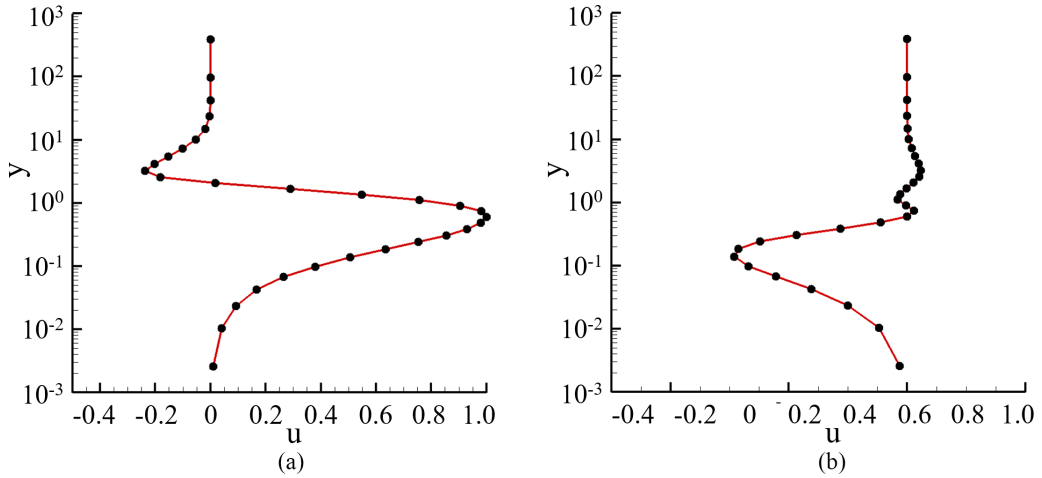

FIG. 10. Comparison of eigenfunction distribution of the streamwise velocity fluctuation, (a) real part, and (b) imaginary part. Solid line: result of this paper; symbols: result of Collis [62].

The results of the stability theory are shown in Fig. 12. With increasing of frequency [Fig. 12(a)], the growth rate of the unstable mode in the shear layer has a maximum value around $\omega = 2.0$ for both two-dimensional ($\beta = 0$) and three-dimensional ($\beta > 0$) disturbances. This indicates that there is a selection mechanism of the frequency in the instability of the shear layer. The selected frequency is around $\omega = 2.0$, and the corresponding physical frequency is $f = \frac{\omega a_\infty}{2\pi h} \approx 11\,000$ Hz. Figure 13 shows the schematic of the detection points $P1$ (early stage near the nozzle exit) and $P2$ (rapid instability stage) in the shear layer and corresponding power spectral density analysis results of the density fluctuations. There is a dominant frequency near $f = 10\,000$ Hz at both positions. This dominant frequency agrees well with the prediction of LST and the DMD results later in this paper.

Further insight into the Fig. 12(b), near the selected frequency $\omega = 2.0$, there is a maximum growth rate at spanwise wave number $\beta = 4.5$. The corresponding spanwise wavelength $\lambda_z = \frac{2\pi h}{\beta} = 1.4h$, which agrees well with the numerical result [seen in Fig. 7(a)] $\lambda_z = 1.25h$. To

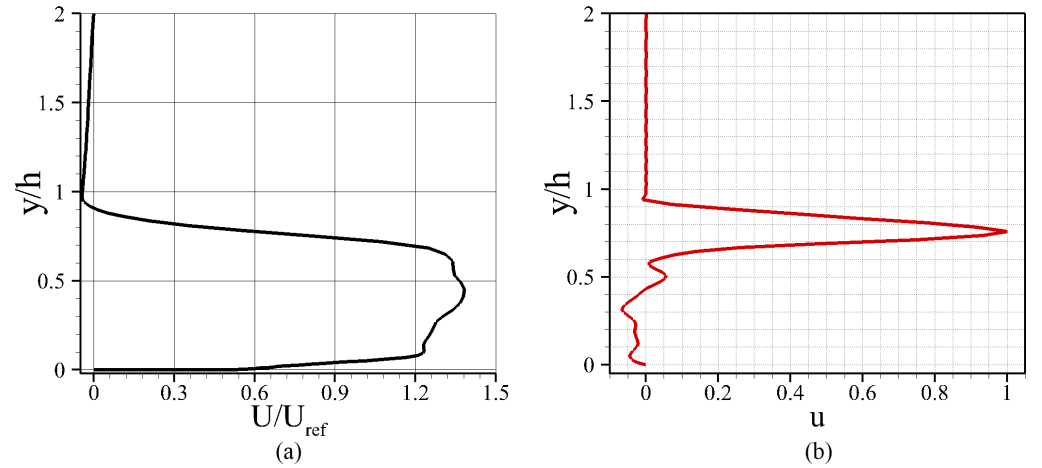

FIG. 11. (a) Velocity profile for linear stability analysis and (b) eigenfunction distribution of the streamwise velocity disturbance for the unstable mode in shear layer.

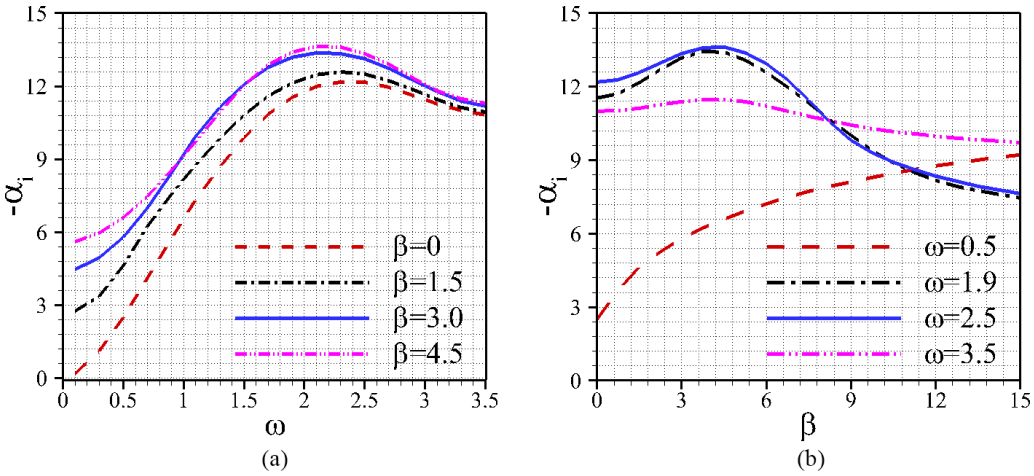

FIG. 12. Curve of (a) growth rate with frequency and (b) growth rate with spanwise wave number.

summarize, it can be considered that the dominant frequency and spanwise wavelength of the disturbances in the shear layer are selected by the nozzle exit condition.

B. Secondary instability

1. Roll-mode

In the ensemble averaged view, pairs of counter-rotating streamwise vortices are located on the flanks of the low-speed streaks as shown in Fig. 7(a). This counter-rotating mode is known to be associated with the symmetric (varicose) mode secondary instability of the streaks based on the understanding from boundary layer studies [25–27,35]. However, by employing conditional averaged sorting technology, Kevin *et al.* [44,45] have found that the counter-rotating secondary roll-mode accounts for only 15% of the instantaneous fields, while the one-sided patterns are 32%. Hence, they concluded that caution should be applied when portraying or reconstructing instantaneous

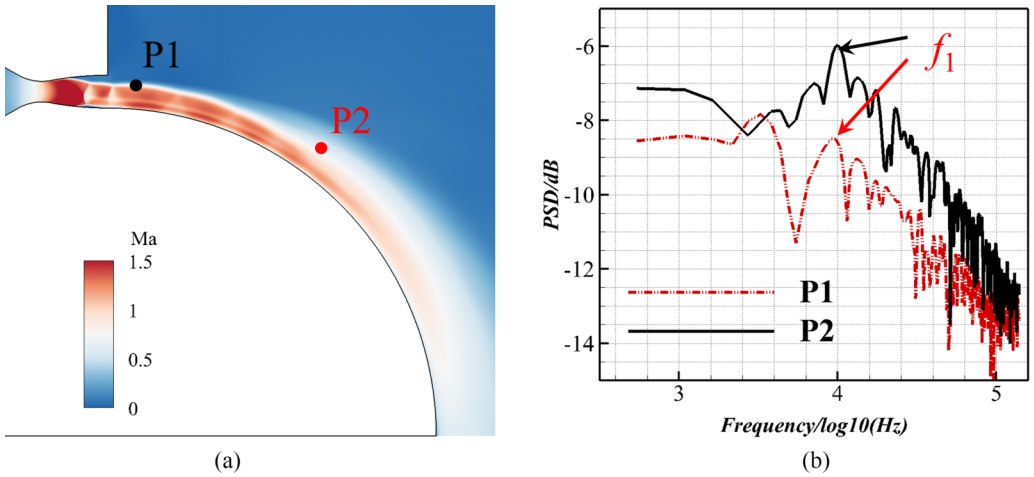

FIG. 13. Schematic of detection points P1 and P2 and density fluctuations power spectral density analysis results.

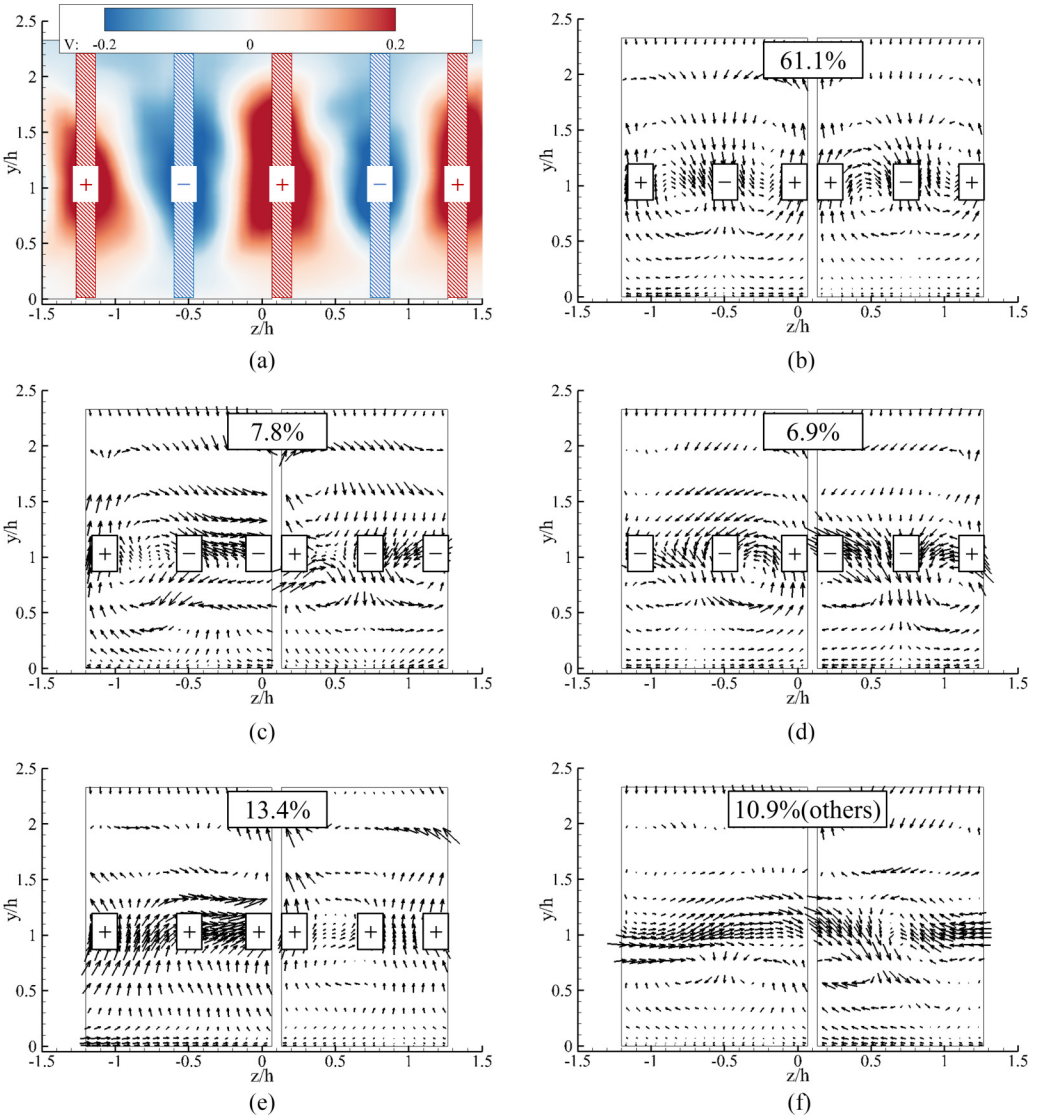

FIG. 14. (a) Illustration of areas where the radial velocities are average to determine the common radial-flow directions at $\theta = 45^\circ$. (b) Conditionally averaged vectors when the averaged radial velocity is $+, -, +$, which represents the counter-rotating mode. [(c) and (d)] Conditionally averaged vectors when the averaged radial velocities are $+, -, -$ and $-, -, +$, respectively, which represent one-sided patterns. [(e) and (f)] Conditionally averaged vectors for the remaining patterns.

flow fields using a representative structure with enforced symmetry, since it may obscure certain attributes that are of dynamical significance to the instantaneous turbulence structure.

Here, by using the similar sorting technology to Kevin *et al.* [44,45], we aim to evaluate how the instantaneous streamwise vortices appear in the compressible shear layer of the jet over a convex wall. This sorting method is based on the average of the instantaneous radial velocity at the center of alternating high- and low-speed streaks in spanwise direction. The filtered radial velocity is averaged within a spanwise length of $0.1\lambda_z$ as illustrated in Fig. 14(a) (hatched region) to determine the instantaneous sign of the radial flow in these regions. Different roll-modes are then

TABLE I. Percentage of different roll-modes with various streamwise locations.

Locations	Roll-modes				
θ	$+,-,+$	$+,-,-$	$-,-,+$	$+,+,+$	Others
$\theta = 25^\circ$	88.9%	0.0%	0.0%	11.1%	0.0%
$\theta = 35^\circ$	86.1%	0.6%	0.4%	12.5%	0.5%
$\theta = 45^\circ$	61.1%	7.8%	6.9%	13.4%	10.9%
$\theta = 65^\circ$	27.8%	10.8%	11.6%	18.3%	31.4%
$\theta = 75^\circ$	19.6%	11.3%	11.5%	20.7%	37.0%

sorted based on the sign of the low-speed streak and two neighbor high-speed streaks combination, giving eight possibilities for each low-speed streak. It is applied to all eight low-speed streaks and only two are shown in Fig. 14; the proportions of each mode in Figs. 14(b) to 14(f) are the results of counting all eight low-speed streaks. For example, the illustration in Fig. 14(a) shows a positive-negative-positive or $(+, -, +)$ pattern, which represents a counter-rotating flow pattern. For this, conditionally averaged view of the cross-flow vectors can be produced for this pattern as shown in Fig. 14(b). The counter-rotating vortices appear as expected, and this pattern accounts for 61.1% of all instantaneous flow fields, while the one-sided flow modes ($-, -, +$ and $+, -, -$) shown in Figs. 14(c) and 14(d) present 14.7% at the streamwise location $\theta = 45^\circ$. The remaining patterns of $(+, +, +)$ and others contain 24.4%.

The above conditional average analysis is then repeated at other several streamwise locations, and the results are presented in Table I. In the initial stage, the counter-rotating mode($+, -, +$) dominates the development of the shear layer and accounts for more than 85%. There are few one-sided patterns($-, -, +$ and $+, -, -$) in the remaining modes. Following the evolution of the shear layer downstream at $\theta = 45^\circ$, the proportion of the counter-rotating mode decreases but still dominates (accounting for 61.1%), and the influence of the one-sided patterns gradually appears (accounting for 14.7%). Finally, in the self-similar region ($\theta > 60^\circ$), the proportion of various roll-modes tends to be equal, which indicates that turbulence in the shear layer is fully developed.

2. Secondary instability mode

The above analysis of the roll-modes has revealed that the counter-rotating mode is dominated in the transient stage of the shear layer in this study. In addition, hairpin vortex has also been observed in the instantaneous flow field shown in Fig. 9. Thus, it is expected that the secondary instability here is dominated by the symmetric (varicose-type) mode based on the secondary instability studies in the boundary layer [29,30].

In addition to the dominant counter-rotating mode, there are still one-sided patterns with the evolution of the shear layer downstream (Table I). Moreover, the spanwise overlapping of the hairpin vortex legs produces alternating sign change of the streamwise vorticity as shown in Fig. 15. These

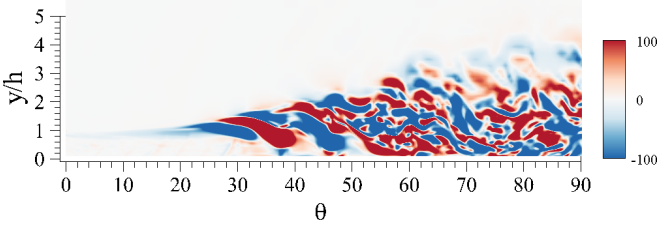

FIG. 15. Streamwise vorticity contours at $z/h = -1.2$, which is located between the high-speed and low-speed streaks.

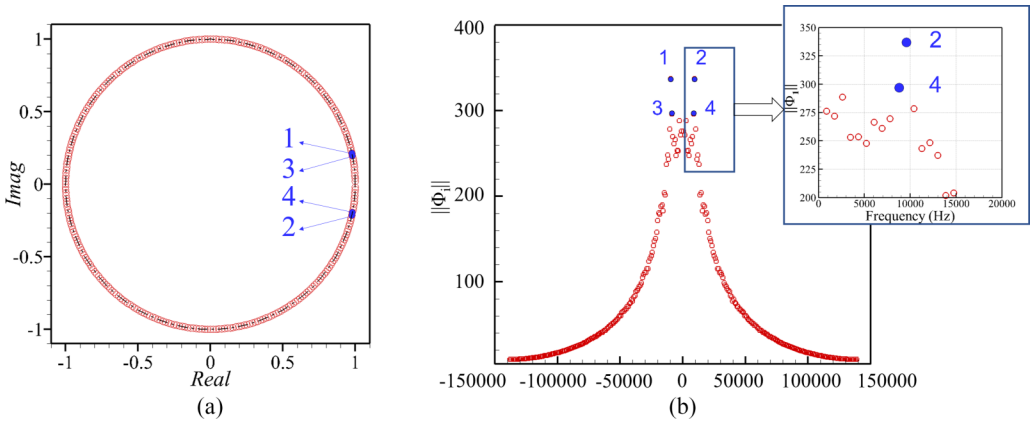

FIG. 16. DMD modes (a), eigenvalue distribution, and (b), energy as a function of frequency.

quasistreamwise vortices with vorticity of alternate signs are well known to be associated with the antisymmetric (sinuous-type) secondary instability mode [29,30]. Therefore, it is expected that there would be a combination and competition of both varicose and sinuous mode secondary instabilities.

Furthermore, a widely applicable data-driven modal decomposition method, DMD [41], is performed on the spanwise velocity fluctuation of the instantaneous snapshots to investigate the secondary instability in the shear layer. The eigenvalue distribution and the energy of the DMD mode as a function of frequency are shown in Fig. 16. As expected, the modal energy decreases with the increase of frequency (except in the small range of low frequencies) since higher frequencies are always associated with smaller-scale coherent structures. The first two pairs of conjugate modes with the highest energy are marked in Fig. 16. The eigenvalue distribution shows that all modes are very close to the unit circle in the complex plane, meaning that the growth or decay rates are close to zero. The spatial distributions of the marked modes are shown in Fig. 17. There are backward-tilted alternating positive and negative spanwise velocity fluctuations regions in the streamwise direction, which indicates that the streaks sway in the spanwise direction, that is, the secondary instabilities. Moreover, the time evolutions of these modes at the cross-stream plane $\theta = 35^\circ$ are shown in Fig. 18 and Fig. 19. The positive and negative values of this mode are just opposite in half a period. Focusing on the spatial distributions of the modes in Fig. 18, the spanwise fluctuations on the flanks of the low-speed regions are the same signs, which could induce the side-to-side sway motion of the

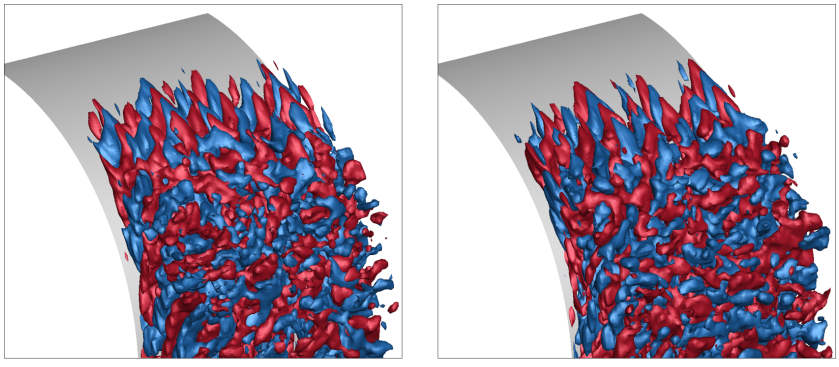

(a) Conjugate modes 1 and 2 (b) Conjugate modes 3 and 4

FIG. 17. Spatial distributions of the DMD modes, isosurfaces show the positive (red) and the negative (blue) spanwise velocity fluctuation.

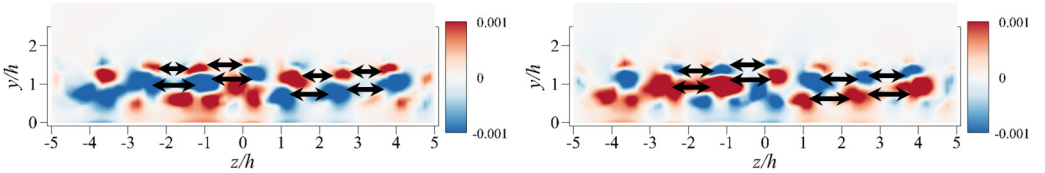

FIG. 18. Time evolution of the conjugate modes 1 and 2 at cross-stream plane $\theta = 35^\circ$. The arrows point to the spanwise velocity fluctuations with the same signs on the flank of low-speed streaks.

streaks. This indicates that the conjugate modes 1 and 2 are the sinuous-type secondary instability. On the contrary, the low-speed streaks in Fig. 19 have opposite spanwise fluctuations on both sides, which leads to periodic thickening and thinning motions of the low-speed streaks. This indicates that the conjugate modes 3 and 4 are the varicose-type secondary instability. To summarize, there are both sinuous- and varicose-type secondary instabilities in the shear layer, and competitions between these modes would occur.

In order to quantitatively evaluate the proportion of the two secondary instability modes in the low-speed streaks of the shear layer, the sorting method from Kevin *et al.* [44,45] is also employed for the areas illustrated in Fig. 20. The areas are located on the flanks of the low-speed streaks to determine the spanwise fluctuation directions. Different instability modes can be sorted by detecting the averaged spanwise velocity fluctuation direction. For example, if the averaged spanwise velocity fluctuation at the left-hand side (dash box) is positive, and the right-hand side (solid box) is negative, then the corresponding low-speed region exhibits thinness motion. This positive-negative mode $(+, -)$, together with another negative-positive mode $(-, +)$, is called the varicose mode. In such an instability mode, the low-speed region exhibits alternating thinning and thickening motions. Similarly, the negative-negative mode $(-, -)$ and positive-positive mode $(+, +)$ are referred to as the sinuous mode, which makes the low-speed region sway side to side. Figures 21 and 22 depict the conditionally averaged streamwise velocity contours of the varicose and sinuous secondary instability mode, respectively. It can be observed that the low-speed regions thinning and thickening motion caused by the varicose mode, and side-to-side sway motion induced by the sinuous mode.

The aforementioned conditional average analysis is repeated at various streamwise locations, and the results for proportions of different secondary instability modes are shown in Table II. As the shear layer evolves downstream from $\theta = 25^\circ$ to 45°, the proportion of the varicose mode decreases from 84.4% to 50.6%, and, accordingly, the sinuous mode increases from 15.6% to 49.4%. This indicates that the secondary instability of the shear layer is dominated by the varicose mode at the initial stage, and then transits to a competition of these two modes. This result is consistent with the previous conclusion on the roll-modes and the instantaneous large-scale coherent structures.

The change of secondary instability modes proportions can be explained from the following two aspects. On the one hand, the initial stage of shear layer development is dominated by the counter-rotating roll-mode and symmetric hairpin vortex, which is associated with the varicose-type

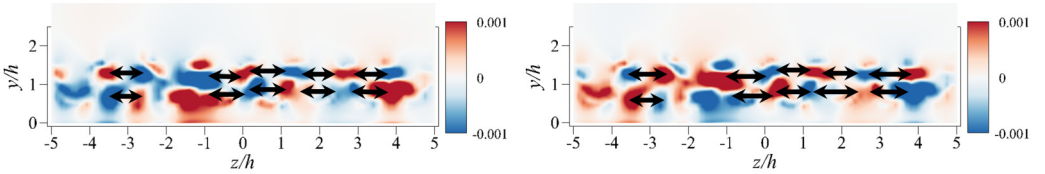

FIG. 19. Time evolution of the conjugate modes 3 and 4 at cross-stream plane $\theta = 35^\circ$. The arrows point to the spanwise velocity fluctuations with opposite signs on the flank of low-speed streaks.

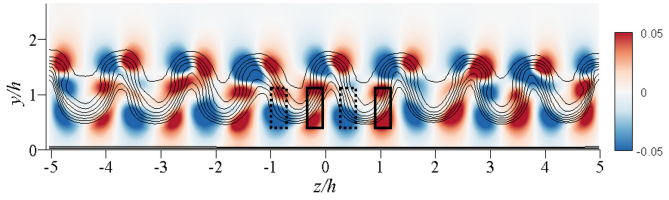

FIG. 20. Illustration of areas where the spanwise velocity fluctuations are averaged to determine the common spanwise fluctuation directions at $\theta = 35^\circ$ (solid and dash boxes). The color contours show the spanwise velocity. The background lines display the underlying streak profile using streamwise velocity, and levels vary from 0 to 1.0.

instability. Then the one-sided roll-mode appears, and the overlapping of the hairpin vortex legs in the spanwise direction produces the quasistreamwise vortices with vorticity of alternate sign, which means the prominence of the sinuous-type instability mode. On the other hand, experimental and numerical studies on the near-wall low-speed streak by Swearingen *et al.* [29] and Asai *et al.* [30] concluded that the sinuous modes are less affected by the diffusion of the streak mean shear and are amplified for a longer streamwise distance. Also, Asai *et al.* [30] studied the influence of streak width and found that, compared to the varicose mode, the sinuous instability is relatively more important for the narrow streak. In terms of the low-speed streak in this study, the width almost keeps a constant value in the instability region as shown in Fig. 23(a). While the thickness of the shear layer increases exponentially in this region as shown in Fig. 23(b). The vorticity thickness of the shear layer grows by nearly 2.5 times from a streamwise position of 25° to 45°, that is, the relative width of the low-speed streaks narrows. The sinuous-type instability mode plays a more and more important role in the narrower streak based on the conclusion of Asai *et al.* [30].

3. Instability mechanism and energy extraction from the mean flow

Figures 24(a) and 24(b) show the rms value distributions of the streamwise velocity fluctuations in the cross-stream plane at $\theta = 35^\circ$ for the conditional averaged varicose mode and sinuous mode, respectively. For the varicose mode, the streamwise velocity fluctuations are largest in the downwash region where the radial shear takes the maximum and on the flanks of the low-speed streak where the spanwise shear is maximum. This distribution of the varicose mode is consistent with that in the boundary layer secondary instability reported by Swearingen *et al.* [29] and Asai *et al.* [30]. For the sinuous mode, the largest fluctuations are distributed on the flanks of the low-speed streaks but not in the region of the highest spanwise shear as in the boundary layer streak [25,29,30]. This observation will be explained below.

In order to examine the instability mechanism and turbulent energy extraction from the mean flow, the distribution of the turbulent kinetic energy production in the cross-stream (y, z) plane is evaluated, where turbulent kinetic energy production term $P_k = (-\overline{u'v'}\frac{\partial U}{\partial y}) + (-\overline{u'w'}\frac{\partial U}{\partial z})$. The first

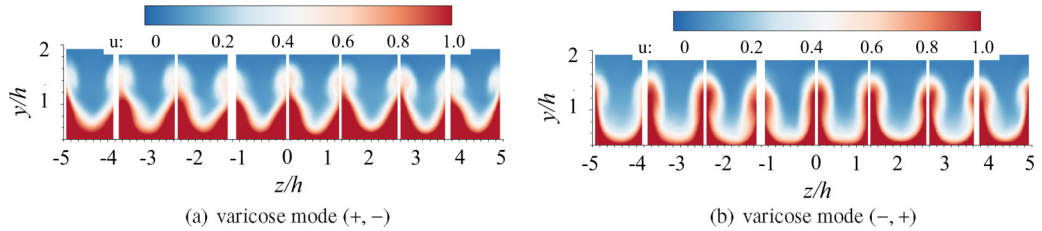

(a) varicose mode (+, −) (b) varicose mode (−, +)

FIG. 21. Streamwise velocity contours of the varicose mode at $\theta = 35^\circ$.

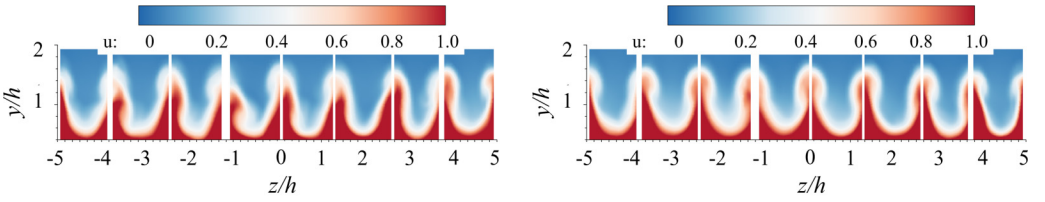

(a) sinuous mode (−, −) (b) sinuous mode (+, +)

FIG. 22. Streamwise velocity contours of the sinuous mode at $\theta = 35^\circ$.

term $T_y = -\overline{u'v'}\frac{\partial U}{\partial y}$, represents the Reynolds shear stress $\overline{u'v'}$ act against the mean shear in the radial direction $\frac{\partial U}{\partial y}$, while the second term, $T_z = -\overline{u'w'}\frac{\partial U}{\partial z}$, is associated with the work of the Reynolds shear stress $\overline{u'w'}$ on the spanwise shear $\frac{\partial U}{\partial z}$. In fact, in centrifugally unstable flow, it is well known that the varicose mode has been understood as an instability of the inflection points generated by the wall-normal variation of streamwise velocity, whereas the spanwise shear is responsible for the sinuous mode instability. However, Brandt *et al.* [30] have found that the turbulent energy production associated with the wall-normal shear is one order of magnitude larger than that associated with its spanwise counterpart in the sinuous mode instability. Therefore, they concluded that it is not always correct to relate the sinuous instability to the streak spanwise shear and the varicose modes to the streak wall-normal shear. Here Fig. 25 shows the distributions of turbulent energy production terms associated with the radial and spanwise shear for the conditionally averaged varicose and sinuous mode. By comparing with the streamwise velocity gradient in Fig. 14, the largest turbulent energy productions are found to correspond with the maximum radial and spanwise shear. Moreover, it is worth noting that both varicose and sinuous modes are affected by radial and spanwise shear components of the turbulent energy production term, and they are in the same order of magnitude. That is, as Brandt *et al.* [30] concluded, it is inappropriate to simply attribute the varicose modes to the wall-normal shear and sinuous instability to the spanwise shear.

The turbulent energy production distributions in Fig. 25 seem to be wrapped around the boundary of the low-speed streaks. Brandt *et al.* [30] proposed a local reference coordinate system to explain this distribution. The local reference system is defined as (x, n, p), where x is the streamwise direction, n is the direction parallel to the basic flow velocity gradient, defined by $\tan\phi = \frac{\partial U/\partial z}{\partial U/\partial y}$, and b is the third orthogonal axis satisfying the right-hand rule. In this local system, the turbulent energy production term $T_p = -\overline{u'_x u'_p}\frac{\partial U}{\partial p} = 0$ according to the definition of this system. Thus, the production of the turbulent energy is only owing to the shear stress $\overline{u'_x u'_n}$ act on the local mean shear $\frac{\partial U}{\partial n}$. The distributions of this term are shown in Fig. 26. It can be noted that they correspond with the cross-stream distributions of the fluctuations in Fig. 24, which indicates that the mechanism of the instability is due to the velocity fluctuations and Reynolds stress parallel to the local mean flow gradient, whether in the varicose mode or sinuous mode. The local inflection point instability caused by the mean flow gradient is also the source of turbulent energy that sustains the instabilities.

TABLE II. Percentage of different secondary instability modes with various streamwise locations.

Locations	Varicose mode		Sinuous mode	
θ	+, −	−, +	−, −	+, +
$\theta = 25^\circ$	45.20%	39.20%	7.20%	8.40%
$\theta = 35^\circ$	40.10%	26.20%	16.40%	17.30%
$\theta = 45^\circ$	23.60%	27.00%	24.60%	24.80%

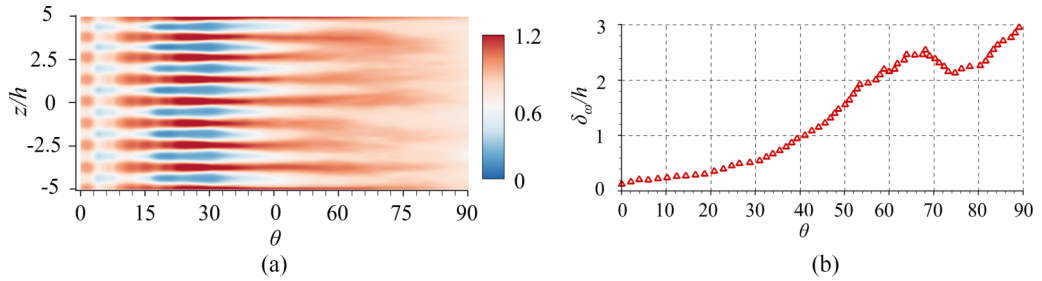

FIG. 23. (a) Mean streamwise velocity contours at $y/h = 0.75$, which shows the high- and low-speed steaks in the shear layer. (b) Vorticity thickness development of the shear layer.

V. CONCLUDING REMARKS

In the present study, the secondary instabilities in the shear layer of the compressible jet over a convex wall were investigated by using the DDES method based on the SST turbulence model. The primary conclusions of this study are summarized as follows.

Taylor-Görtler-type centrifugal instability induces the generation of the streamwise vortices in the shear layer of the convex wall jet. By the activity of the streamwise vortices, there are spanwise periodic upwash and downwash regions, that is, alternating high-speed and low-speed streaks. The streaks would exhibit secondary instabilities as those in other wall-bounded shear flows under the influence of the inflection points in the spanwise and radial directions.

The LST method developed by S. Scott Collis [62] with consideration of the compressible and curvature effects is employed to predict the dominant frequency and spanwise wavelength of the disturbances in the shear layer. They agree well with the numerical results. This indicates that the dominant frequency and spanwise wavelength of the disturbances in the shear layer are selected by the nozzle exit condition. Moreover, it is worthwhile and meaningful to use other nonlinear analysis methods, such as secondary instability theory, parabolic stability equations, and global instability analysis to study the instability of the compressible jet over a convex wall.

The observation of the vortex structures has revealed that the hairpin vortices are the dominant large coherent structures in the transient stage of the shear layer. Moreover, the roll-modes of the streaks are quantitatively evaluated using a conditionally averaged sorting technology similar to that in Kevin *et al.* [44,45]. The results demonstrate that the counter-rotating mode is dominated in the transient stage of the shear layer. The hairpin vortices and the counter-rotating mode are often associated with the symmetric (varicose-type) secondary instability mode. However, as the shear layer evolves downstream, there still are one-sided roll patterns (accounting for 14.7% at $\theta = 45°$). Also, the spanwise overlapping of the hairpin vortex legs produces quasistreamwise vortices with

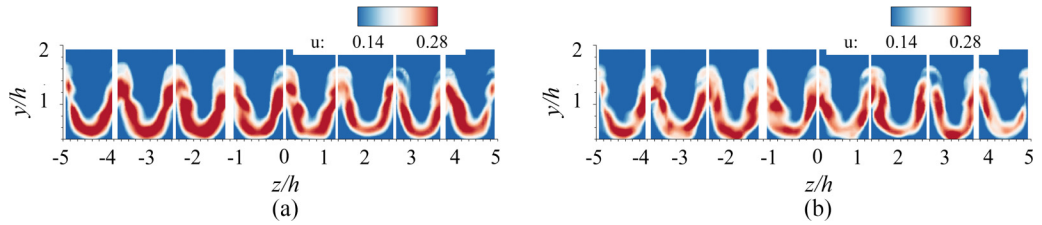

FIG. 24. Streamwise fluctuation of the conditionally averaged (a) varicose mode and (b) sinuous mode extracted at $\theta = 35°$.

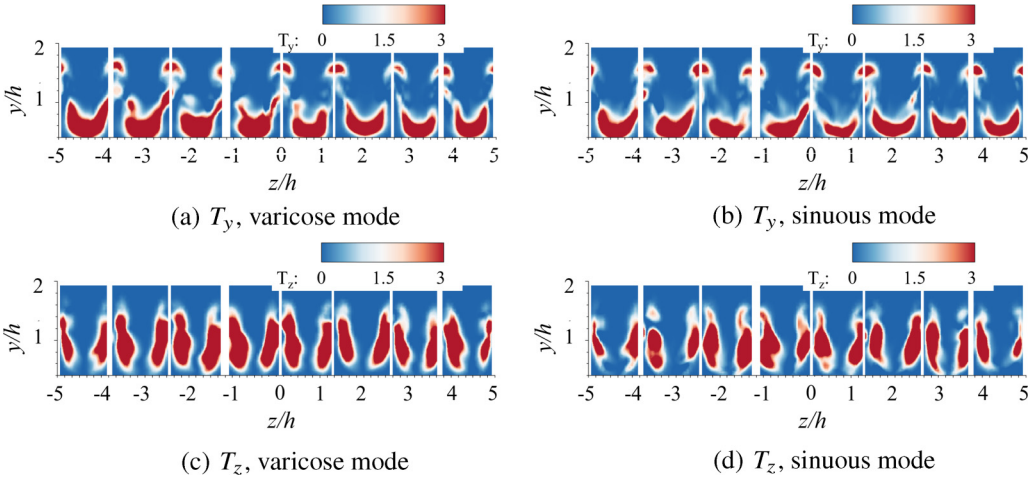

FIG. 25. Turbulent kinetic energy production of the conditionally averaged [(a) and (c)] varicose mode and [(b) and (d)] sinuous mode extracted at $\theta = 35^\circ$.

vorticity of alternate sign, which is well known to be related to the antisymmetric (sinuous-type) secondary instability mode.

The DMD analysis of the spanwise velocity fluctuation has revealed that secondary instabilities of both the sinuous- and varicose-types exist in the shear layer, and competitions between these modes would occur. The conditionally averaged sorting method is also used to quantitatively evaluate the competition of secondary instability modes. The sorting results observed the thinning and thickening motions induced by the varicose mode, as well as the side-to-side sway motions caused by the sinuous mode. As the shear layer evolves downstream from $\theta = 25^\circ$ to 45°, the proportion of the varicose mode decreases from 84.4% to 50.6%, and, accordingly, the sinuous mode increases from 15.6% to 49.4%. This is consistent with the previous conclusions from the roll-modes and instantaneous large-scale coherent structures analyses. The variation in the proportions of the secondary instability modes is caused by the diffusion of the streak mean shear, and the exponential increase of the shear layer thickness, which results in a relatively narrower streak.

Based on the analysis of the turbulent kinetic energy production terms, the Reynolds shear stresses $\overline{u'v'}$ against the mean shear in the radial direction $\partial U/\partial y$ and $\overline{u'w'}$ on the spanwise shear $\partial U/\partial z$, which are of equal magnitude, are the causes of both the varicose and sinuous modes. Thus, it is inappropriate to simply attribute the sinuous instability to the spanwise shear and the varicose modes to the wall-normal shear. Further, according to a local reference coordinate system analysis, the mechanism of the instability is due to the velocity fluctuations and Reynolds stress parallel to the

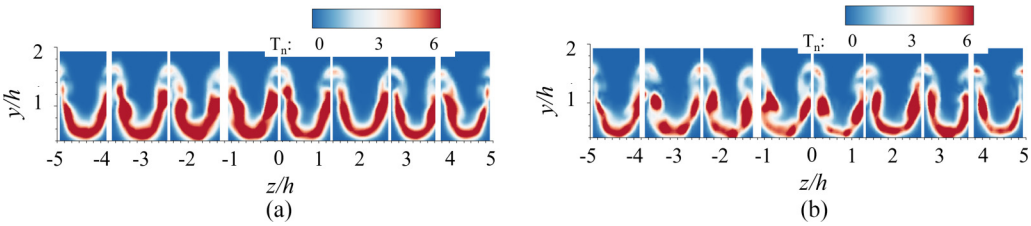

FIG. 26. Turbulent kinetic energy production of the conditionally averaged (a) varicose mode and (b) sinuous mode extracted at $\theta = 35^\circ$.

local mean flow gradient. The local inflection point instability induced by the mean flow gradient is also the source of turbulent energy that sustains the instabilities.

ACKNOWLEDGMENTS

This study was co-supported by the National Natural Science Foundation of China (Grants No. 11972308 and No. 11902265) and the National Major Basic Research Project 1912.

[1] C. Henri, Device for deflecting a stream of elastic fluid projected into an elastic fluid, U.S. Patent (Google Patents, 1936).
[2] C. Warsop and W. J. Crowther, Fluidic flow control effectors for flight control, AIAA J. **56**, 3808 (2018).
[3] C. Warsop, W. Crowther, and M. Forster, Nato avt-239 task group: Supercritical coanda based circulation control and fluidic thrust vectoring, in *AIAA Scitech 2019 Forum* (AIAA, Reston, VA, 2019), p. 0044
[4] D. R. Smith and C. Warsop, Nato avt-239 task group: 'Innovative control effectors for manoeuvring of air vehicles'—Introduction and overview, in *AIAA Scitech 2019 Forum* (AIAA, Reston, VA, 2019), p. 0041.
[5] W. J. Crowther, P. I. A. Wilde, K. Gill, and S. M. Michie, Towards integrated design of fluidic flight controls for a flapless aircraft, Aeronaut. J. **113**, 699 (2009).
[6] P. Wilde, A. Buonanno, W. Crowther, and A. Savvaris, Aircraft control using fluidic maneuver effectors, in *26th AIAA Applied Aerodynamics Conference* (AIAA, Reston, VA, 2008), p. 6406.
[7] C. Hutchin, Nato avt-239 task group: Control effectiveness and system sizing requirements for integration of fluidic flight controls on the saccon aircraft configuration, in *AIAA Scitech 2019 Forum* (AIAA, Reston, VA, 2019), p. 0280.
[8] D. R. Williams, J. Seidel, R. Osteroos, and T. E. McLaughlin, Nato avt-239 task group: Flight control derivatives using active flow control effectors on the ice/saccon uas model, in *AIAA Scitech 2019 Forum* (AIAA, Reston, VA, 2019), p. 0043.
[9] G. Hoholis, R. Steijl, and K. Badcock, Circulation control as a roll effector for unmanned combat aerial vehicles, J. Aircr. **53**, 1875 (2016).
[10] C. Harley, P. Wilde, and W. Crowther, Application of circulation control manoeuvre effectors for three axis control of a tailless flight vehicle, in *47th AIAA Aerospace Sciences Meeting including The New Horizons Forum and Aerospace Exposition* (AIAA, 2009), p. 146.
[11] R. J. Englar, R. A. Hemmerly, D. W. Taylor, W. H. Moore, V. Seredinsky, W. Valckenaere, and J. A. Jackson, Design of the circulation control wing stol demonstrator aircraft, J. Aircr. **18**, 51 (1981).
[12] J. Yubiao, Z. Liu, H. Yong, G. Lihua, and C. Hong, Lift response characteristics of a circulation control airfoil with internally blown flap, Acta Aeronaut. Astronaut. Sin. **39**, 121807 (2018).
[13] M. G. Alexander, S. G. Anders, S. K. Johnson, J. P. Florance, and D. F. Keller, Trailing edge blowing on a two-dimensional six-percent thick elliptical circulation control airfoil up to transonic conditions, Tech. Rep. NASA/TM-2005-213545 (2005).
[14] Y. Tsuji, Y. Morikawa, T. Nagatani, and M. Sakou, The stability of a two-dimensional wall jet, Aeronaut. Q. **28**, 235 (1977).
[15] S. Wernz and H. F. Fasel, Nonlinear resonances in a laminar wall jet: Ejection of dipolar vortices, J. Fluid Mech. **588**, 279 (2007).
[16] R. Neuendorf and I. Wygnanski, On a turbulent wall jet flowing over a circular cylinder, J. Fluid Mech. **381**, 1 (1999).
[17] T. Watanabe and K. Nagata, Large-scale characteristics of a stably stratified turbulent shear layer, J. Fluid Mech. **927**, A27 (2021).
[18] H. Görtler, Instabilitat laminarer grenzchichten an konkaven wanden gengenuber gewissen deeidimensionalen storungen, Z. Angew. Math. Mech. **21**, 250 (1941).
[19] C. L. Cunff and A. Zebib, Nonlinear spatially developing görtler vortices in curved wall jet flow, Phys. Fluids **8**, 2375 (1996).

[20] O. J. E. Matsson, Görtler vortices in wall jet flow on a rotating cylinder., Phys. Fluids **10**, 2238 (1998).
[21] S. Dong, Direct numerical simulation of turbulent taylor–couette flow, J. Fluid Mech. **587**, 373 (2007).
[22] P. M. Ligrani and R. D. Niver, Flow visualization of dean vortices in a curved channel with 40 to 1 aspect ratio, Phys. Fluids **31**, 3605 (1988).
[23] J. M. Floryan and W. S. Saric, Stability of gortler vortices in boundary layers, AIAA J. **20**, 316 (1982).
[24] H. T. Kim, S. J. Kline, and W. C. Reynolds, The production of turbulence near a smooth wall in a turbulent boundary layer, J. Fluid Mech. **50**, 133 (1971).
[25] P. Andersson, L. Brandt, A. Bottaro, and D. Henningson, On the breakdown of boundary layer streaks, J. Fluid Mech. **428**, 29 (2001).
[26] Y. Konishi and M. Asai, Development of subharmonic disturbance in spanwise-periodic low-speed streaks, Fluid Dyn. Res. **42**, 035504 (2010).
[27] P. Schlatter, L. Brandt, H. C. De Lange, and D. Henningson, On streak breakdown in bypass transition, Phys. Fluids **20**, 101505 (2008).
[28] J. D. Swearingen and R. F. Blackwelder, The growth and breakdown of streamwise vortices in the presence of a wall, J. Fluid Mech. **182**, 255 (1987).
[29] M. Asai, M. Minagawa, and M. Nishioka, The instability and breakdown of a near-wall low-speed streak, J. Fluid Mech. **455**, 289 (2002).
[30] L. Brandt, Numerical studies of the instability and breakdown of a boundary-layer low-speed streak, Eur. J. Mech. B. Fluids **26**, 64 (2007).
[31] W. Eckhaus, *Studies in Non-linear Stability Theory*, Vol. 6 (Springer Science & Business Media, New York, 2012).
[32] Y. Guo and W. H. Finlay, Splitting, merging and wavelength selection of vortices in curved and/or rotating channel flow due to eckhaus instability, J. Fluid Mech. **228**, 661 (1991).
[33] N. Fujisawa and R. Kobayashi, Turbulence characteristics of wall jets along strong convex surfaces, Int. J. Mech. Sci. **29**, 311 (1987).
[34] O. Likhachev, R. Neuendorf, and I. Wygnanski, On streamwise vortices in a turbulent wall jet that flows over a convex surface, Phys. Fluids **13**, 1822 (2001).
[35] R. Neuendorf, L. Lourenco, and I. Wygnanski, On large streamwise structures in a wall jet flowing over a circular cylinder, Phys. Fluids **16**, 2158 (2004).
[36] G. Han, M. D. Zhou, and I. Wygnanski, On streamwise vortices and their role in the development of a curved wall jet, Phys. Fluids **18**, 095104 (2006).
[37] L. Dunaevich and D. Greenblatt, Stability and transition on a coand cylinder, Phys. Fluids **32**, 084106 (2020).
[38] A. Pandey and J. W. Gregory, Instabilities and turbulence in a forced turbulent convex wall jet, Phys. Fluids **32**, 095111 (2020).
[39] J. L. Lumley, The structure of inhomogeneous turbulent flows, in *Atmospheric Turbulence and Radio Wave Propagation* (Nauka, Moscow, 1967), pp. 166–178.
[40] A. Pandey and J. W. Gregory, Spanwise wavelength of streamwise vortices in a forced turbulent convex wall jet, AIAA J. **58**, 1 (2021).
[41] P. J. Schmid, Dynamic mode decomposition of numerical and experimental data, J. Fluid Mech. **656**, 5 (2010).
[42] Q. Wang, F. Qu, D. Sun, and J. Bai, Numerical study of instabilities and compressibility effects on supersonic jet over a convex wall, J. Fluid Mech. **954**, A6 (2023).
[43] P. R. Spalart, S. Deck, M. L. Shur, K. D. Squires, M. K. Strelets, and A. Travin, A new version of detached-eddy simulation, resistant to ambiguous grid densities, Theor. Comput. Fluid Dyn. **20**, 181 (2006).
[44] K. Kevin, J. P. Monty, H. L. Bai, G. Pathikonda, B. Nugroho, J. M. Barros, K. T. Christensen, and N. Hutchins, Cross-stream stereoscopic particle image velocimetry of a modified turbulent boundary layer over directional surface pattern, J. Fluid Mech. **813**, 412 (2017).
[45] K. Kevin, J. Monty, and N. Hutchins, The meandering behaviour of large-scale structures in turbulent boundary layers, J. Fluid Mech. **865**, R1 (2019).

[46] F. Qu and D. Sun, Investigation into the influences of the low-speed flows' accuracy on rans simulations, Aerosp. Sci. Technol. **70**, 578 (2017).
[47] D. Sun, F. Qu, C. Liu, F. Yao, and J. Bai, Numerical study of the suction flow control of the supersonic boundary layer transition in a framework of gas-kinetic scheme, Aerosp. Sci. Technol. **109**, 106397 (2021).
[48] F. Qu, D. Sun, K. Han, J. Bai, G. Zuo, and C. Yan, Numerical investigation of the supersonic stabilizing parachute's heating loads, Aerosp. Sci. Technol. **87**, 89 (2019).
[49] D. Sun, F. Qu, and C. Yan, An effective flux scheme for hypersonic heating prediction of re-entry vehicles, Comput. Fluids **176**, 109 (2018).
[50] F. Qu, J. Chen, D. Sun, J. Bai, and G. Zuo, A grid strategy for predicting the space plane's hypersonic aerodynamic heating loads, Aerosp. Sci. Technol. **86**, 659 (2019).
[51] Q. Wang, F. Qu, Q. Zhao, and J. Bai, Numerical study of the hysteresis effect on the supercritical airfoil for the transonic circulation control, Aerosp. Sci. Technol. **126**, 107645 (2022).
[52] F. R. Menter, Two-equation eddy-viscosity turbulence models for engineering applications, AIAA J. **32**, 1598 (1994).
[53] X. D. Liu, S. Osher, and T. Chan, Weighted essentially non-oscillatory schemes, J. Comput. Phys. **115**, 200 (1994).
[54] S. Yoon and A. Jameson, Lower-upper symmetric-gauss-seidel method for the euler and navier-stokes equations, AIAA J. **26**, 1025 (1988).
[55] A. Llopis-Pascual, Supercritical coanda jets for flight control effectors, Ph.D. thesis, Manchester University, Manchester, 2017.
[56] P. Behrouzi and J. McGuirk, High speed jet plume experimental study: Phase 2/Part1 – RRLU-1 nozzle, full experimental results, Department of Aeronautical Automoblie Engineering Report TT09R02-A (2009).
[57] P. C. Wang and J. J. Mcguirk, Large eddy simulation of supersonic jet plumes from rectangular con-di nozzles, Int. J. Heat Fluid Flow **43**, 62 (2013).
[58] D. Papamoschou and A. Roshko, The compressible turbulent shear layer: an experimental study, J. Fluid Mech. **197**, 453 (1988).
[59] D. W. Bogdanoff, Compressibility effects in turbulent shear layers, AIAA J. **21**, 926 (1983).
[60] N. D. Sandham, Three-dimensional simulations of large-eddies in compressible mixing layer, J. Fluid Mech. **224**, 133 (1991).
[61] D. Zhang, J. Tan, and H. Li, Structural characteristics of supersonic mixing enhanced by introducing streamwise vortices, Appl. Phys. Lett. **111**, 114103 (2017).
[62] S. S. Collis, A computational investigation of receptivity in high-speed flow near a swept leading-edge, Ph.D. thesis, Stanford University, 1997.